RSC Advances

PAPER

View Article Online
View Journal | View Issue

Cite this: *RSC Adv.*, 2020, **10**, 40035

From "S" to "O": experimental and theoretical insights into the atmospheric degradation mechanism of dithiophosphinic acids†

Zhipeng Wang,‡[a] Yixiang Zhang,‡[b] Jingjing Liu,[b] Lianjun Song,[a] Xueyu Wang,[a] Xiuying Yang,[a] Chao Xu,[c] Jun Li*[b] and Songdong Ding*[a]

Dithiophosphinic acids (DPAHs, expressed as R_1R_2PSSH) are a type of sulfur-donor ligand that have been vastly applied in hydrometallurgy. In particular, DPAHs have shown great potential in highly efficient trivalent actinide/lanthanide separation, which is one of the most challenging tasks in separation science and is of great importance for the development of an advanced fuel cycle in nuclear industry. However, DPAHs have been found liable to undergo oxidative degradation in the air, leading to significant reduction in the selectivity of actinide/lanthanide separation. In this work, the atmospheric degradation of five representative DPAH ligands was investigated for the first time over a sufficiently long period (180 days). The oxidative degradation process of DPAHs elucidated by ESI-MS, ^{31}P NMR, and FT-IR analyses is $R_1R_2PSSH \rightarrow R_1R_2PSOH \rightarrow R_1R_2POOH \rightarrow R_1R_2POO{-}OOPR_1R_2$, $R_1R_2PSSH \rightarrow R_1R_2PSS{-}SSPR_1R_2$, and $R_1R_2PSSH \rightarrow R_1R_2PSOH \rightarrow R_1R_2POS{-}SOPR_1R_2$. Meanwhile, the determination of pK_a values through pH titration and oxidation product by PXRD further confirms the S → O transformation in the process of DPAH deterioration. DFT calculations suggest that the hydroxyl radical plays the dominant role in the oxidation process of DPAHs and the order in which the oxidation products formed is closely related to the reaction energy barrier. Moreover, nickel salts of DPAHs have shown much higher chemical stability than DPAHs, which was also elaborated through molecular orbital (MO) and adaptive natural density portioning (AdNDP) analyses. This work unambiguously reveals the atmospheric degradation mechanism of DPAHs through both experimental and theoretical approaches. At the application level, the results not only provide an effective way to preserve DPAHs but could also guide the design of more stable sulfur-donor ligands in the future.

Received 17th October 2020
Accepted 23rd October 2020

DOI: 10.1039/d0ra08841b

rsc.li/rsc-advances

Introduction

Separation of trivalent actinides (An^{3+}) over trivalent lanthanides (Ln^{3+}) is one of the most critical and challenging steps in spent fuel reprocessing owing to their very similar chemical and physical properties.[1,2] Previous reports indicate that An^{3+} and Ln^{3+} could be effectively separated using soft N-donor or S-donor ligands.[3–5] In comparison with N-donor ligands, the S-donor ligands have shown much higher selectivity for An^{3+}/Ln^{3+} separation.[4] For example, the purified CYANEX® 301, which is a typical aliphatic substituted dithiophosphinic acid (DPAH, expressed as R_1R_2PSSH) ligand, could selectively extract Am^{3+} over Eu^{3+} with high separation factors ($SF_{Am/Eu}$) up to 5900 in HNO_3 solution at pH 3.5–4.0.[5] However, when CYANEX® 301 was exposed to oxidation environment such as atmosphere or HNO_3 for a certain time, significant decreases of its selectivity to Am^{3+} over Eu^{3+} could be observed, which is expected to limit its use in real applications.[6,7]

To uncover the underlying chemical mechanism accounted for the decrease of An^{3+}/Ln^{3+} selectivity by DPAHs and help improve the stability of dithiophosphinic acids, a few investigations have been carried out on the oxidation behavior of DPAHs in aqueous solution. It has been shown that a high concentration of non-oxidizing mineral acid such as H_2SO_4 and HCl hardly had obvious detrimental influence on the structure of CYANEX® 301, whereas the oxidizing HNO_3 could destruct the ligand rapidly even at low acidity and for a short testing time.[8,9] With respect to the oxidation products and the possible oxidation pathways of the aliphatic substituted DPAH, there are still different understandings and insights. Wang *et al.* discovered the formation of monothiophosphinic acid (RRPOSH) as the degradation product of $(n\text{-pentyl})_2PSSH$ and $(n\text{-butyl})_2PSSH$

[a]*College of Chemistry, Sichuan University, Chengdu 610064, China. E-mail: dsd68@163.com*

[b]*Department of Chemistry, Key Laboratory of Organic Optoelectronics, Molecular Engineering of the Ministry of Education, Tsinghua University, Beijing 100084, China*

[c]*Collaborative Innovation Center of Advanced Nuclear Energy Technology, Institute of Nuclear and New Energy Technology, Tsinghua University, Beijing 100084, China*

† Electronic supplementary information (ESI) available: Characterization data of all compounds; data of extraction and theoretical calculations. See DOI: 10.1039/d0ra08841b

‡ These authors contributed equally to the work.

in the case of contacting with 1.0 mol L^{-1} or 3.0 mol L^{-1} HNO_3 for 10 hours *via* ^{31}P NMR and FT-IR analyses.[10] However, Menoyo *et al.* proposed that CYANEX® 301 could be oxidized to RRPSOH, RRPS, RRPOOH and RRPO after contacting with 5.0 mol L^{-1} HNO_3 for 10 days using FT-IR, FT-Raman and GC-MS monitorings.[11] The oxidation pathway was afforded as follow: RRPSSH → RRPSOH → RRPOOH. Nevertheless, a further study by Marc *et al.* indicated the formation of dimer product of CYANEX® 301 in contact with 1.0 mol L^{-1} HNO_3 for 18 hours by means of ^{31}P NMR spectra and single crystal analyses,[12] which was also supported by Groenewold *et al. via* ESI-MS spectra and collision-induced dissociation spectra tests.[13] The assessing oxidation pathway was presented as RRPSSH → RRPSS–SSPRR → RRPOS–SOPRR → RRPOO–OOPRR → RRPO–O–OPRR. So far, there has been no scientific consensus about the oxidation mechanism of DPAH.

The stability properties of aromatic group substituted DPAHs have also been studied. $(ClPh)_2PSSH$ is one of the most representative structures of aromatic DPAHs. Modolo *et al.* performed the hydrolysis experiments of $(ClPh)_2PSSH$ in 0.5–3.0 mol L^{-1} HNO_3, HCl, or H_2SO_4.[14] It was found that $(ClPh)_2$-PSSH decomposed completely after contacting with 3.0 mol L^{-1} HNO_3 for more than 20 days. To avoid this adverse impact, reducing agents or radical scavengers such as amidosulfuric acid, urea, or hydrazine must be added into the biphasic extraction system.[15,16] However, this stabilizing method has led to a more complex extraction system and, unfortunately, did not completely solve the problem of oxidative degradation of DPAHs. Moreover, it was also found DPAH could be oxidized in ambient environment.[17,18] For example, CYANEX® 301 could degrade obviously in 3 hours when exposed to the air. In contrast, this ligand would be very stable in an inert atmosphere, suggesting that DPAH are very sensitive to the oxidizing atmosphere. This oxidation issue in ambient environment not only deteriorate the extraction performances of DPAHs, but also requires special protection measures during their transportation and storage, which in turn limits their applications in advanced fuel cycle. Therefore, investigation on DPAH oxidation behavior at ambient environment is of great significance. Unfortunately, to the best of our knowledge, data are very scarce on the oxidation stability of DPAHs at ambient environment. As a result, the understanding on the oxidation processes of DPAHs at ambient environment is superficial due to the lack of sufficient experimental evidences and theoretical supports.

In the present work, by taking consideration of the impact of substituent on the oxidation, five representative DPAHs (Fig. S1†) bearing different alkyl and/or aryl substituent groups were intentionally synthesized and their oxidation processes were systematically monitored at ambient environment for 180 days using ESI-MS, ^{31}PNMR, FT-IR, PXRD, and pH titration methods. Meanwhile, along with the oxidation of DPAHs, the extraction behavior of Am^{3+} and Eu^{3+} by these ligands was also investigated. Moreover, a detailed oxidation mechanism of DPAHs was proposed through the help of density functional theory and *ab initio* study.

Experimental section

General

The radioactive trace solution of $^{241}Am^{3+}$ with radionuclidic purity was supplied by China Institute of Atomic Energy. The HNO_3 solution containing Eu^{3+} was prepared from $Eu_2O_3 \cdot 6H_2O$ (99.99%, Aldrich, USA). All the other reagents used in this work were of AR grade and used as received. 85% aqueous H_3PO_4 was utilized as external standard for ^{31}P NMR. The investigated ligands of this work were prepared by referring to previous literature.[19]

The ESI-MS spectra were collected on Bruker Amazon SL spectrometer (Bruker Inc., Switzerland). ^{31}P NMR spectra were recorded by Varian Inova NMR spectrometer (240 MHz) (Bruker Inc., Switzerland). FT-IR spectra were recorded on Nicolet 6700 Fourier transform infrared spectrometer (Thermo Fisher Scientific Inc., USA). Powder X-ray diffraction (PXRD, Shimadzu 6100, Japan) patterns were obtained using Cu Kα radiation (0.1542 nm) at 40 kV and 30 mA. The Lei Ci PHS-3C type pH meter (Shanghai Precision & Scientific Instrument Co. Ltd., China) was used for determining pK_a values of DPAH compounds as well as pH values of aqueous phase. The NaI(Tl) scintillation counter (China National Nuclear Inc., China) was used for detecting the radioactivity of $^{241}Am^{3+}$ in each phase. The inductively coupled plasma atomic emission spectrometer (ICP-AES, IRIS Advantage, Thermo Elemental Inc., USA) was applied to determining the concentration of Eu^{3+} in aqueous phase.

Oxidation procedures

Adequate amount of each DPAH sample was separately placed in $\Phi = 3.5$ cm open beaker and exposed to the ambient environment. 20 μL aliquots were withdrawn from each sample for ESI-MS, ^{31}P NMR, FT-IR characterizations and pK_a values determination with appropriate time intervals. The solid oxidation product was successively filtered from the sample, washed with ethanol and dried in oven prior to the PXRD test.

pH titration

0.75 mmol DPAH was dissolved in EtOH/H_2O (99/1%, v/v) mixture (50 mL) and titrated by 0.05 mol L^{-1} NaOH aqueous solution at 25.0 ± 0.5 °C. The pH values were recorded with pH meter. Each ligand was titrated in triplicates. The pK_a values were determined through the stepwise linear regression method[20,21] and the purity of examined compounds was also calculated.

Extraction

The DPAH ligands were dissolved in toluene to obtain the organic phase with a concentration of 0.5 mol L^{-1} DPAH. The aqueous phase with different concentrations of HNO_3 contains trace amount of $^{241}Am^{3+}$, 200 ppm Eu^{3+}, and 1.0 mol L^{-1} $NaNO_3$. Equal volumes of the two phases were stirred thoroughly at 25.0 ± 0.5 °C for 30 min to ensure phase transfer equilibrium. After phase separation by centrifugation, 0.5 mL specimens of each

phase was pipetted into test tubes. The radiocounts of $^{241}Am^{3+}$ in both organic phase and aqueous phase were measured separately. The concentration of Eu^{3+} in aqueous phase was analyzed by ICP-AES. The distribution ratio (D) for $^{241}Am^{3+}$ and Eu^{3+} was defined as the ratio of metal ion concentration in the organic phase ($[M]_{org.}$) to that in the aqueous phase ($[M]_{aq.}$), $D_M = [M]_{org.}/[M]_{aq.}$. The separation factor ($SF_{Am/Eu}$) was expressed as the ratio of D_{Am} and D_{Eu}, $SF_{Am/Eu} = D_{Am}/D_{Eu}$.

Theoretical calculations

The substituent groups of all the reactants in the experiment do not participate in the reactions, so methyl was used to replace the alkyl or aryl groups in order to improve the calculation efficiency. The simplified dithiophosphonic acids were labeled as MeDPAH in the following discussions. The structures of reactants, intermediates, transition states and products were optimized by B3LYP functions (density functional theory) combining with the 6-311++G(d,p) basis set using Gaussian 09 Program.[22] The harmonic vibrational analyses were conducted to confirm the minima character of the obtained geometries at the same level of theory (*i.e.* the local minimal with positive frequencies and the saddle points with only one imaginary frequency). The intrinsic reaction coordinates (IRC)[23] calculations were performed to confirm that the transition states connect the designated reactants and products. In order to obtain the highly accurate relative energies, single-point energies of all the optimized stationary point optimized at the B3LYP/6-311++G(d,p) level of theory were refined using CCSD(T) method[24] in combination with 6-311++G(d,p) basis set. If it is not otherwise specified, all the relative energies mentioned below are calculated from CCSD(T)/6-311++g(d,p) level of theory. Gibbs free energy was calculated with single point energies calculated from CCSD(T)/6-311++g(d,p) level and the sum of zero-point energy corrections and entropy corrections. Translational and rotational entropies are neglected for solid state substance. The software of CYLview[25] was used to draw the geometric structures of the stationary points on the potential energy surface (PES).

The hydroxyl radical has been recognized as the most important oxidant in the atmosphere, which always acts as initiator of oxidation and degradation of organic compound.[26–32] As a result, the hydroxyl radical was also considered as the main oxidant for the oxidation of these dithiophosphonic acids investigated in this work. It is noted that, the effects of oxygen and water molecules in the atmospheric degradation of MeDPAH were also considered. However, these reactions were not competitive with respect to the reactions with hydroxyl radical. Therefore, we only detailed the reaction mechanism of hydroxyl radical with MeDPAH below, and the other reactions were presented in the ESI.†

The $Ni(MeDPA)_2$ complex was fully optimized using the Amsterdam Density Functional program (ADF2016.106).[33] The generalized gradient approximation (GGA) with the PBE functional and the TZ2P Slater type basis set[34] were used for all atoms. The scalar-relativistic ZORA formalism was adopted to account for the relativistic effects.[35,36] In order to gain further insights into the chemical bonds of $Ni(MeDPA)_2$, we performed AdNDP analysis to generate the multi-centered localized orbitals using Multiwfn codes.[37]

Results and discussion

Identification of oxidation products

The oxidation products of DPAHs were identified with the help of spectroscopic techniques including ESI-MS, ^{31}P-NMR, FT-IR, *etc.* For clarity, the following discussions mainly focus on the results of one representative DPAH L_1, which shows the most obvious changes during the oxidation experiment.

The oxidative degradation process of DPAHs was strictly monitored by ESI-MS. The ESI-MS spectra of L_1 with oxidation time of 0 d and 180 d are shown in Fig. 1. The numbers in brackets are the generation order of species. Other mass spectra of L_1 with oxidation time of 5 d, 10 d, 20 d, 30 d, 60 d, 90 d, 120 d, and 150 d are summarized in ESI as Fig. S2.† As we can see, the pure ligand L_1 with molecule formula of R_1R_2PSSH can be observed at m/z = 287.1057. After 180 days oxidation, several oxidation products successively appeared at m/z = 271.1285, 571.1880, 255.1514, 539.2336, and 507.2793, which can be attributed to R_1R_2PSOH, $R_1R_2PSS–SSPR_1R_2$, R_1R_2POOH, $R_1R_2POS–SOPR_1R_2$, and $R_1R_2POO–OOPR_1R_2$, respectively.[12,13,16,17] The emergence of different types of impurities means that DPAH can degrade not only through the replacement of sulphur atom by oxygen atom, but also *via* coupling reaction to form dimers. This result indicates that the appearance of both oxo-substitute monomer and coupling-dimer of the previous works is possible even the oxidation environment is not exactly the same. Regularly, all of the products were observed step by step, in the sequence of $R_1R_2PSSH \rightarrow R_1R_2PSOH \rightarrow R_1R_2POOH \rightarrow R_1R_2POO–OOPR_1R_2$, $R_1R_2PSSH \rightarrow R_1R_2PSS–SSPR_1R_2$, and $R_1R_2PSSH \rightarrow R_1R_2PSOH \rightarrow R_1R_2POS–SOPR_1R_2$, severally. Meanwhile, ESI-MS spectra of L_2–L_5 (Fig. S3–S6 in ESI†) show the same variation process as L_1, revealing the common degradation regularities of DPAH ligands in air atmosphere. Even so, it should be noted that the occurrence time of new decomposition species is different for each ligand. Specifically, the first oxidative product R_1R_2PSOH appeared at 5 d for L_1, whereas that of L_2, L_3, L_4, and L_5 is 20 d, 10 d, 10 d, and

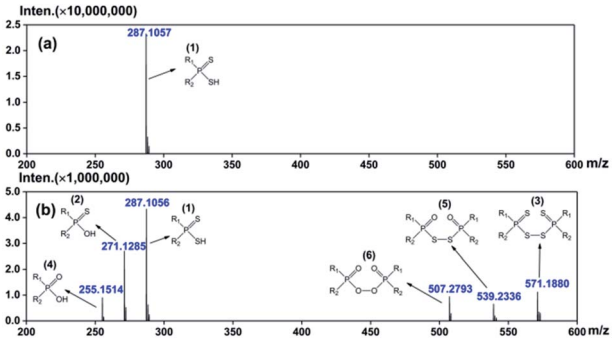

Fig. 1 ESI-MS spectra of L_1 at ambient environment for 0 d (a) and 180 d (b).

20 d, separately. In addition, the appearance time of the last oxidative species is 90 d for L_1, 150 d for L_2, 120 d for L_3, 120 d for L_4, and 180 d for L_5. Herein, the stability of five ligands can be preliminarily arranged as follows: $L_5 > L_2 > L_4 \approx L_3 > L_1$.

The ^{31}P NMR spectra of L_1 with different oxidation degrees are shown in Fig. 2(a). It is clear that the decomposition species increase with the extension of testing time. The signal peaks at 62.12, 86.32, 71.95, 58.26, 72.71, and 73.85 ppm are assigned to R_1R_2PSSH, R_1R_2PSOH, $R_1R_2PSS–SSPR_1R_2$, R_1R_2POOH, $R_1R_2POS–SOPR_1R_2$, and $R_1R_2POO–OOPR_1R_2$, respectively,[10–12,14,16,17] which coincided with the occurrence order of mass spectra. Further, the ratios of each product can be roughly calculated through the integrals of corresponding peaks and shown in Fig. 2(b). It can be seen that proportions of the impurities grow with the increasing of oxidation time. After degradation of 180 days, only 31% of the pure L_1 is left. Whilst the residual ratios of pure L_2, L_3, L_4, and L_5 are 49%, 38%, 41%, and 64%, severally (Fig. S7–S10 in ESI†). The above intercomparison reveals that the stabilities of ligands are correlated with the variation in substituents. The DPAH molecules attached with *o*-trifluoromethyl phenyl (L_5, L_2, and L_4) show good resistance to the air, indicating that the introduction of *o*-trifluoromethyl phenyl group is conducive to the air oxidation resistance. On the basis of ESI-MS and ^{31}P NMR analyses, L_5 is considered as the most stable ligand.

To further determine the molecular structure of the oxidation products, we examined the ligands by FT-IR spectroscopy in succession. Spectra of L_1–L_5 are presented as Fig. S11 in ESI.† The variations in the IR spectra are rather complicated. Nonetheless, some regularities on the functional groups evolution can be summarized. The characteristic peaks of P═S at 631 cm^{-1} and 501 cm^{-1} gradually flatted with the extension of exposure time in the air.[9,11,38] At the same time, the peaks distributed from 1000 cm^{-1} to 1280 cm^{-1} become more obvious, which can be attributed to the formation of P═O and P–OH functional groups. Beyond the general phenomena of L_1–L_5, some detailed distinctions have also been captured. In the spectra of L_1, L_3, L_4, and L_5, peaks ascribed to P═S ranging from 750 cm^{-1} to 830 cm^{-1} disappear gradually, indicating the reduction of R_1R_2PSSH molecules. Besides, the P–OH absorptions in the spectra of L_2, L_3, and L_4, distributed in the range of 870 cm^{-1} to 985 cm^{-1}, become stronger over the examined time, which further reveals the replacement of sulfur by oxygen during oxidation. Moreover, an unusual band belonging to S–S group vibration was observed near 480 cm^{-1} in the graphs of L_3 and L_4, indicating the occurrence of coupling reaction during degradation.

In the process of the experiment, slight rotten egg smell diffused from the samples, which may demonstrate the generation of hydrothion (H_2S). In addition, the color of L_1 and L_3 changed from dark green to light yellow, whereas L_2, L_4, and L_5 with the color of orange get darker over the measurement period. Interestingly, yellow solid separated out from the samples (Fig. S12†), which is speculated to be sulfur. For further analysis of the precipitate composition, the yellow solid was characterized by PXRD and compared with the diffraction standard spectrogram of sulfur. Corresponding characterization results are shown in Fig. S13.† The diffraction peaks of the test sample match with those of the simulated rhombic sulfur[39] very well, proving the formation of S powder during the degradation of DPAHs.

As a phosphonic acid ligand, structural changes may have effects on its properties, such as the degree of H^+ dissociation. Thus, the variation on the pK_a values of five ligands was also recorded in the examined 180 d. As can be seen from Fig. 3, all the pK_a values of the five ligands increase with the extension of monitoring time, which further indicates the replacement of S atom by O atom during the oxidation.[40] Through a comparison, the ΔpK_a values between 0 d and 180 d of five ligands are

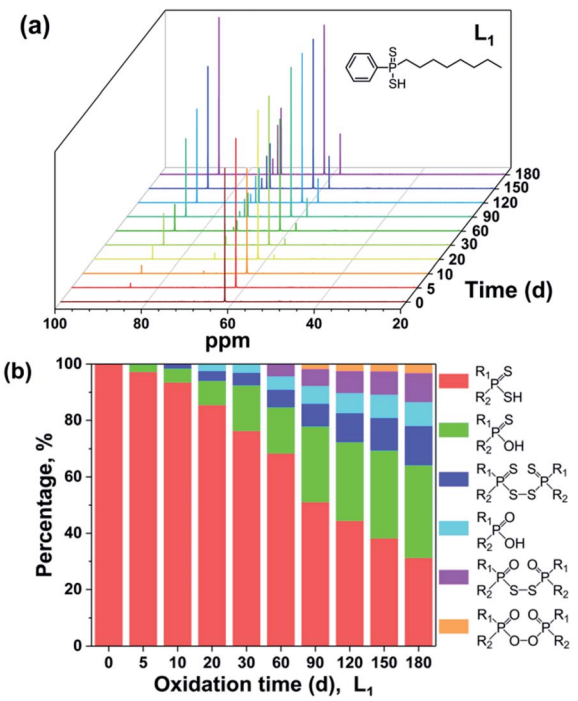

Fig. 2 ^{31}P NMR spectra (a) and percentages of oxidation products (b) of L_1 at ambient environment for different oxidation time.

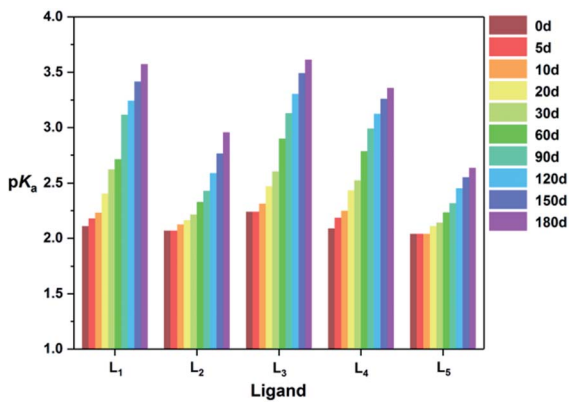

Fig. 3 pK_a values of L_1–L_5 at ambient environment for different oxidation time.

sequenced as $L_5 > L_2 > L_4 \approx L_3 > L_1$, which is in accordance with the foregoing experimental results.

Influence of DPAH oxidation on extraction

The degradation of DPAH extractants may have effect on their extraction behavior. Thus, the influence of oxidation time on the extraction of Am^{3+} and Eu^{3+} by the five DPAHs was investigated. The D values and $SF_{Am/Eu}$ values of L_1–L_5 at different time are shown in Fig. S14,† respectively. Both D_{Am} and D_{Eu} increase more than one magnitude after 180 days degradation, which originate from the strong extractability of coordinated oxygen atom transformed from sulfur atom.[6,7] Besides, the increase in D_{Eu} is more obvious than D_{Am}, leading to the decrease of separability. After 180 days oxidation, the $SF_{Am/Eu}$ values of L_1–L_5 decrease from 9.5 to 2.9, 150 to 23, 1060 to 16, 17 to 1.6, and 1800 to 150, respectively. The changes on the $SF_{Am/Eu}$ values of DPAH ligands imply that air oxidation does have great influence on the extraction of Am^{3+} and Eu^{3+}. In the meantime, five DPAHs show different resistance abilities to the air. Among the investigated ligands, L_5 still holds a high $SF_{Am/Eu}$ values over 100 even oxidized by air for 180 days, exhibiting a good potential application prospects in the future.

Preservation of DPAHs

During the synthesis of DPAH ligands, the crude product was converted to nickel salt form for recrystallization. Then the Ni-salt was acidized by HCl to obtain the target ligand with satisfying purity.[19] Intriguingly, we found that all the Ni-salts of the investigated ligands were still very pure after placing in the ambient environment for 180 days (Fig. S15†). It means that the transformation of DPAH ligand to Ni-salt can reduce the reactiveness of ligand oxidation effectively. More importantly, it will provide a convenient preservation method of DPAH ligand with great significance. We consider that the formation of coordination bond S···Ni···S can stabilize the compound, preventing degradation of ligand even in contact with the air directly. Actually, this view point can be accepted due to the fact that sulphur acts as a proton acceptor and tends to form a more stable complex with divalent 3 d transition metal ions such as nickel or cobalt.[41,42] The detailed analysis by theoretical calculation has been performed in the latter section.

Oxidation mechanism

To understand and explain the details of the oxidation reaction in a molecular level, the reactions of MeDPAH with hydroxyl radical, oxygen and water were calculated theoretically, respectively. Here, the Gibbs free energy surface for the reaction between MeDPAH and hydroxyl radical were displayed (Fig. 4, S16 and S17†) owing to its competitive advantage in reaction kinetics.[26] The profiles for the other reactions were presented in ESI as Fig. S19–S21.†

According to the order of intermediates generation in the whole oxidation process, the entire reaction mechanism is divided into three stages. In each stage, three different reaction pathways have been considered, which are filled in black, red, and blue for visual differentiation. As indicated by the black

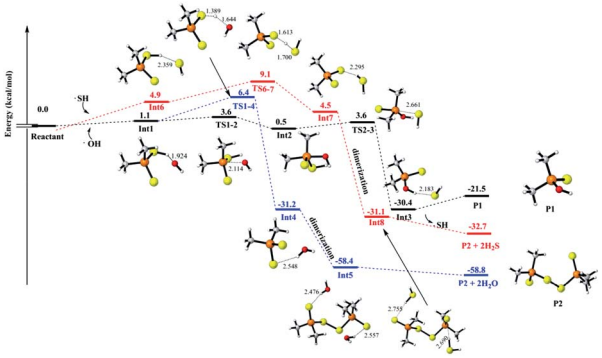

Fig. 4 Gibbs free energy profile from MeDAPH to generate P1 (R_1R_2PSOH) and P2 (R_1R_2PSS–$SSPR_1R_2$) at CCSD(T)/6-311++G(d,p)//B3LYP/6-311++G(d,p) level (in kcal mol^{-1}). The name of species is labeled below and the corresponding energy is labeled above. The unit of bond length is angstrom.

path in Fig. 4, the reaction initiates from hydrogen bonded complex Int1, which locates 1.1 kcal mol^{-1} higher than the total energy of the initial reactant. As the reaction proceeds, Int1 connects to intermediate Int2 *via* transition state TS1-2, where the hydroxyl radical adds to the phosphorous atom with an energy barrier of 2.4 kcal mol^{-1}. As Int2 forms, the reaction proceeds to pass through an energy barrier of 3.2 kcal mol^{-1} to produce a hydrogen-bonded complex Int3 *via* TS2-3. The SH radical leaves *via* the cleavage of P–SH bond in TS2-3 to generate Int3, followed by the production of P1 (R_1R_2PSOH) which is the first oxidation product detected in experiment. The first oxidation stage is accompanied by the substitution of SH in MeDPAH with OH to produce P1, where the cleavage of P–SH bond with 3.2 kcal mol^{-1} energy barrier is the rate-determined step.

Alternatively, the reaction can proceed *via* hydrogen abstraction reaction to produce Int4 (the blue path). In TS1-4, the hydrogen transfers from sulfur atom to oxygen atom with an energy barrier of 5.3 kcal mol^{-1}. Once Int4 forms, it will get together immediately with the existing hydrated $(CH_3)_2PS_2$ radical to produce Int5 followed by leaving of H_2O to produce P2 (R_1R_2PSS–$SSPR_1R_2$). P2 is the second oxidation intermediate detected in experiment with the total energy barrier of 6.4 kcal mol^{-1}.

As we all know, most radicals have very high reaction activity, so the byproduct SH radical[43,44] produced in the reaction path labeled in black was also considered as one of the oxidants in the whole reaction pathways, which has been depicted in Fig. 4, S16 and S17† in red path. As shown in Fig. 4, the SH radical approaches the initial reactant to form a hydrogen bond complex Int6 with a Gibbs free energy of 4.8 kcal mol^{-1} because of entropy decrease. Then the reaction proceeds *via* the similar reaction pathways as that marked in blue. However, this path is different in that the H_2S acts as a kind of byproduct (Fig. 4) instead of H_2O. The generation of H_2S here further confirmed the component of the rotten egg smell gas captured in the experiment.

By comparing the three different ways in Fig. 4, it can be seen that the whole energy barrier for P1 production is 3.6 kcal mol^{-1}

(labeled black), while the energy barrier for P2 production is 6.4 kcal mol^{-1} (labeled blue). The lower energy barrier for P1 production is consistent with the appearance of P1 before P2 in the experiment. It is worth noting that, although the energy barrier for P2 production with the path labeled in red is only 9.0 kcal mol^{-1}, the SH radical is one of the byproducts of the pathway for P1 production. Therefore, the reaction pathway labeled as red will take place after the blue one.

Remarkably, the geometries of P1 are very similar to the reactant, with only one alteration that the thiol was substituted by the hydroxyl. Therefore, as shown in Fig. S16,† the three reaction pathways of forming P3 and P4 from P1 are similar to those shown in Fig. 4. It is worth noting that, for the $(CH_3)_2PS_2$ radical in Int12, the calculated spin density indicates that the single electron is mainly distributed over the sulfur atom (Fig. S18†), so the dimerization of Int12 takes place between two sulfur atom with an barrierless process. This could also explain the detected species $R_1R_2POS–SOPR_1R_2$ instead of $R_1R_2PSO–OSPR_1R_2$ in the experiment. Analogously, the similar three pathways of generating P5 from P4 are depicted in Fig. S17.† All energy barriers of these reaction pathways shown in Fig. 4, S16, and S17† are summarized in Table 1. Coincidentally, it can be seen from Table 1, the black reaction pathways are always more favorable than the red ones in Fig. 4 and S16,† which is consistent with the appearance order of the oxidation products.

Apart from hydroxyl radical, the oxygen and water molecules in the atmosphere might also degrade DPAH ligands to some extent. Thus, the effects of these species were considered, respectively. The oxidation pathways of oxygen are shown in Fig. S19.† The initiate complex Int24, locating at 1.5 kcal mol^{-1} relative to the total energy of DPAH and oxygen, reacts to generate P2 and P5 successively through a series of intermediate products and transition states. Meanwhile, oxysulfide will release in the process of Int27 → Int17, which may be one of the compositions of the pungent gas. In this profile, the whole energy barriers of P2 and P5 are 28.4 kcal mol^{-1} and 65.7 kcal mol^{-1}, respectively, which are much higher than those of hydroxyl radical oxidation route. Therefore, the oxygen oxidation is not competitive. It is noteworthy that the byproduct hydroperoxyl radical is also considered to be an important oxidant in the atmosphere. Thus, the possible oxidation reactions involving hydroperoxyl radical was further analyzed as Fig. S20.† From the calculations, the whole energy barrier of P1 formation is 25.7 kcal mol^{-1}, which is much higher than that of hydroxyl radical oxidation processes. As a result, the oxidation by hydroperoxyl radical is negligible.

Table 1 The summary of all energy barriers of various reaction pathways shown in Fig. 4, S16, and S17 (kcal mol^{-1})

	Energy barriers, (kcal mol^{-1})		
Pathway	In Fig. 4	In Fig. S16	In Fig. S17
Black	8.9	9.2	20.7
Blue	5.3	1.2	20.3
Red	9.1	11.3	28.9

In addition to the oxygen, the effect of water molecule in degrade process was described in Fig. S21.† The whole energy barrier of the generation of P1 is 42.9 kcal mol^{-1}, which is higher than that of hydroxyl radical oxidation obviously. It is worth noting that the concentration of hydroxyl radical in the troposphere is approximately 10.9×10^5 molecules cm^{-3},[45] which is rather low in comparison with that of oxygen and water molecules. However, the generation rate of ˙OH in the atmosphere includes two parts, formation of transient O atom from O_3 by photodissociation and reaction between water vapor and transient O atom.[46] In other words, ˙OH and O_3 are dynamic equilibrated. In this work, the reaction between hydroxyl radical and dithiophosphinic acid molecules can be regarded as an initiation step in the entire oxidation process. With the consumption of hydroxyl radical, new ˙OH will be generated continuously through the ozone-hydroxyl radical dynamic equilibrium. Essentially, the O_3 molecules are actually consumed and hydroxyl radical act as "catalyst" in this process. Besides, the concentration of O_3 is 50–85 ppb by volume in air in Beijing,[47] which is comparable with the content of O_2 and H_2O. Herein, the oxidation by oxygen and water molecules is confirmed as uncompetitive kinetically in comparison with hydroxyl radical.

The stability of $Ni(MeDPA)_2$

The canonical molecular orbital (MO) diagram can give in-depth bonding information which is related to the stability of $Ni(MeDPA)_2$ complexes.[48,49] Fig. 5 presents the MO energy levels calculated at the PBE/TZ2P level of theory. The doubly frontier occupied orbitals 8 b_{3g}, 4 b_{2g}, 19 a_g, and 18 a_g are mainly non-bonding Ni-based 3 d orbitals. Clearly, the occupied bonding MOs 9 b_{1g}, 8 b_{1g}, and 17 a_g show the interaction between Ni and S atoms on both sides. Upon the electron donation from metal to ligand orbitals, the virtual 9 b_{1g} orbital of $(MeDPA)_2$ was significantly stabilized by 3 $d_{x^2-y^2}$ orbital of the central Ni atom to form σ-type bonding. The rest MOs mainly come from $(MeDPA)_2$, little contributed from Ni 3 d orbitals. The 3 d orbital from Ni overlaps with 8 b_{1g} orbital to form the Ni–S σ bond (8

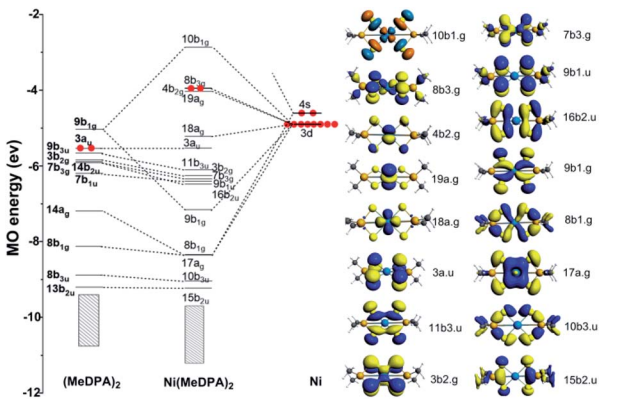

Fig. 5 The MO bonding scheme of D_{2h} $Ni(MeDPA)_2$ at the level of PBE/TZ2P (isovalue = 0.03), illustrating the bonding interactions between $(MeDPA)_2$ and Ni fragments.

b_{1g} MO). Further, the 14 a_g orbital in $(MeDPA)_2$ is significantly stabilized by interacting with 4 s orbital of Ni to form 17 a_g MO (Ni–S σ bond). These three Ni–S σ-type bonds are deeply buried beneath and strongly stabilized with respect to individual MeDPAH molecule (the MO energy levels of MeDPAH are shown in Fig. S22†). Overall, the inherent chemical bonding between Ni and the surrounding ligand is dominantly derived from the 9 b_{1g} orbital, with 10 b_{1g} as its corresponding antibonding counterpart. In addition, each pair of two adjacent sulfurs atoms can form π-type bonds *via* MO 11 b_{3u} and 16 b_{2u}, whereas these bonds are absent in MeDPAH case. These π-type interactions give rise to the considerable decrease of the S⋯S distance from 3.496 in MeDPAH to 3.147 Å in $Ni(MeDPA)_2$.

The chemical bonding in $Ni(MeDPA)_2$ can be further understood by AdNDP analysis.[50,51] As the AdNDP results (the 1c–2e and 2c–2e bonds are not listed) shown in Fig. S23,† there are two 4c–2c π bonds contributed by the S 3p orbitals, and these delocalized bonds strengthen the interactions between the two isolated MeDPA. The remaining delocalized bonds are all in-plane σ bonds. The interactions between Ni and $(MeDPA)_2$ are mainly achieved by 5c–2e σ bonds constituted by S 3p orbitals as well as Ni 4 s and 3 d orbitals, respectively, which hold the whole complex together steadily. Meanwhile, the three 6c–2e σ bonds strengthen the S–P bonds. Overall, because of these delocalized bonds in compound $Ni(MeDPA)_2$, it is difficult to break the S–P or S–Ni bond in the air, determining the high stability of Ni-salts.

Conclusions

For the first time, the oxidation behavior of five DPAH ligands with typical structures at ambient environment was systematically investigated through ESI-MS, ^{31}P NMR, FT-IR, and pH titration. It has been shown that DPAH molecules were oxidized in the following pathways: $R_1R_2PSSH \rightarrow R_1R_2PSOH \rightarrow R_1R_2POOH \rightarrow R_1R_2POO–OOPR_1R_2$, $R_1R_2PSSH \rightarrow R_1R_2PSS–SSPR_1R_2$, and $R_1R_2PSSH \rightarrow R_1R_2PSOH \rightarrow R_1R_2POS–SOPR_1R_2$. The introduction of *o*-trifluoromethyl phenyl group was helpful to improve the oxidation resistance of DPAHs. Along with the oxidation of DPAHs, both D_{Am} and D_{Eu} increased, whereas $SF_{Am/Eu}$ decreased dramatically. Remarkably, the ligand L_5 bearing two *o*-CF_3Ph substituent groups could still effectively separate Am^{3+} over Eu^{3+} after 180 days oxidation, suggesting a good application prospect. Theoretical calculations revealed that the oxidation process of DPAHs was mainly governed by a hydroxyl radical oxidation mechanism. Meanwhile, the order in which the oxidation products formed was closely related to the reaction energy barrier. Due to the stabilization effect of the delocalized bonds, the nickel salt of DPAH showed much better stability as compared to the pure DPAH. In conclusion, the results of this work not only give a rational oxidation mechanism and an effective preservation method for DPAHs at ambient environment, but also provide important guidance to design more stable S-donor ligands for actinide/lanthanide separation in the future.

Conflicts of interest

There are no conflicts to declare.

Acknowledgements

The authors are very grateful for the financial support by the National Science Foundation of China (Grant No. 11675115, 11975161, and 91426302). Comprehensive training platform of specialized laboratory (College of chemistry, Sichuan University) is acknowledged for ESI-MS, ^{31}P NMR, FT-IR, PXRD, and ICP-AES analyses. The calculations were performed using supercomputers at Tsinghua National Laboratory for Information Science and Technology.

References

1 D. Lundberg and I. Persson, *Coord. Chem. Rev.*, 2016, **318**, 131–134.
2 G. T. Seaborg, *Radiochim. Acta*, 1993, **61**, 115–122.
3 C. L. Xiao, C. Z. Wang, L. Y. Yuan, B. Li, H. He, S. A. Wang, Y. L. Zhao, Z. F. Chai and W. Q. Shi, *Inorg. Chem.*, 2014, **53**, 1712–1720.
4 F. W. Lewis, M. J. Hudson and L. M. Harwood, *Synlett*, 2011, **18**, 2609–2632.
5 Y. J. Zhu, J. Chen and R. Z. Jiao, *Solvent Extr. Ion Exch.*, 1996, **14**, 61–68.
6 Y. J. Zhu, J. Chen and G. R. Choppin, *Solvent Extr. Ion Exch.*, 1996, **14**, 543–553.
7 C. Hill, C. Madic, P. Baron, M. Ozawa and Y. Tanaka, *J. Alloys Compd.*, 1998, **271**, 159–162.
8 K. C. Sole, J. Brent Hiskey and T. L. Ferguson, *Solvent Extr. Ion Exch.*, 1993, **11**, 783–796.
9 J. Chen, R. Z. Jiao and Y. J. Zhu, *Solvent Extr. Ion Exch.*, 1996, **14**, 555–565.
10 F. Wang, C. Jia, D. F. Pan and J. Chen, *Ind. Eng. Chem. Res.*, 2013, **52**, 18373–18378.
11 B. Menoyo, M. P. Elizalde and A. Almela, *Anal. Sci.*, 2002, **18**, 799–804.
12 P. Marc, R. Custelcean, G. S. Groenewold, J. R. Klaehn, D. R. Peterman and L. H. Delmau, *Ind. Eng. Chem. Res.*, 2012, **51**, 13238–13244.
13 G. S. Groenewold, D. R. Peterman, J. R. Klaehn, L. H. Delmau, P. Marc and R. Custelcean, *Rapid Commun. Mass Spectrom.*, 2012, **26**, 2195–2203.
14 G. Modolo and S. Seekamp, *Solvent Extr. Ion Exch.*, 2002, **20**, 195–210.
15 C. Madic, F. Testard, M. J. Hudson, J. Liljenzin, B. Christansen, M. Ferrando, A. Facchini, A. Geist, G. Modolo, G. Espartero and J. Mendoza, *CEA-Report 6066*, 2004.
16 M. E. Freiderich, D. R. Peterman, J. R. Klaehn, P. Marc and L. H. Delmau, *Ind. Eng. Chem. Res.*, 2014, **53**, 3606–3611.
17 P. Marc, *Doctoral dissertation*, Oak Ridge National Laboratory, 2011.
18 H. Ma, O. Kökkılıç, C. M. Marion, R. S. Multani and K. E. Waters, *Can. J. Chem. Eng.*, 2018, **96**, 1585–1596.

19 Z. P. Wang, N. Pu, Y. Tian, C. Xu, F. Wang, Y. Liu, L. R. Zhang, J. Chen and S. D. Ding, *Inorg. Chem.*, 2019, **58**, 5457–5467.
20 C. X. Zeng and Q. Hu, *Indian J. Chem., Sect. A: Inorg., Bioinorg., Phys., Theor. Anal. Chem.*, 2008, **47**, 71–74.
21 G. P. Gillman, *Soil Res.*, 1985, **23**, 643–646.
22 M. J. Frisch, G. W. Trucks, H. B. Schlegel, G. E. Scuseria, M. A. Robb, J. R. Cheeseman, G. Scalmani, V. Barone, B. Mennucci, G. A. Petersson, H. Nakatsuji, M. Caricato, X. Li, H. P. Hratchian, A. F. Izmaylov, J. Bloino, G. Zheng, J. L. Sonnenberg, M. Hada, M. Ehara, K. Toyota, R. Fukuda, J. Hasegawa, M. Ishida, T. Nakajima, Y. Honda, O. Kitao, H. Nakai, T. Vreven, J. A. Montgomery Jr, J. E. Peralta, F. Ogliaro, M. Bearpark, J. J. Heyd, E. Brothers, K. N. Kudin, V. N. Staroverov, R. Kobayashi, J. Normand, K. Raghavachari, A. Rendell, J. C. Burant, S. S. Iyengar, J. Tomasi, M. Cossi, N. Rega, J. M. Millam, M. Klene, J. E. Knox, J. B. Cross, V. Bakken, C. Adamo, J. Jaramillo, R. Gomperts, R. E. Stratmann, O. Yazyev, A. J. Austin, R. Cammi, C. Pomelli, J. W. Ochterski, R. L. Martin, K. Morokuma, V. G. Zakrzewski, G. A. Voth, P. Salvador, J. J. Dannenberg, S. Dapprich, A. D. Daniels, O. Farkas, J. B. Foresman, J. V. Ortiz, J. Cioslowski and D. J. Fox, *Gaussian 09, revision C.1*, Gaussian, Inc., Wallingford, CT, 2009.
23 K. Ishida, K. Morokuma and A. Komornicki, *J. Chem. Phys.*, 1977, **66**, 2153–2156.
24 R. J. Bartlett, *J. Chem. Phys.*, 1989, **93**, 1697–1708.
25 C. Y. Legault, *CYLVIEW, 1.0 b*, Université de Sherbrooke, 2009.
26 R. Atkinson, *Atmos. Environ.*, 2000, **34**, 2063–2101.
27 R. Atkinson and J. Arey, *Chem. Rev.*, 2003, **103**, 4605–4638.
28 G. V. Buxton, C. L. Greenstock, W. P. Helman and A. B. Ross, *J. Phys. Chem. Ref. Data*, 1988, **17**, 513–886.
29 M. Gnanaprakasam, L. Sandhiya and K. A. Senthilkumar, *Theor. Chem. Acc.*, 2017, **136**, 131–147.
30 M. Ng, D. K. Mok, E. P. Lee and J. M. Dyke, *J. Phys. Chem. A*, 2017, **121**, 6554–6567.
31 B. Wei, J. Sun, Q. Mei and M. He, *Comput. Theor. Chem.*, 2018, **1129**, 1–8.
32 P. O. Wennberg, K. H. Bates, J. D. Crounse, L. G. Dodson, R. C. McVay, L. A. Mertens, T. B. Nguyen, E. Praske, R. H. Schwantes, M. D. Smarte, J. M. S. Clair, A. P. Teng, X. Zhang and J. H. Seinfeld, *Chem. Rev.*, 2018, **118**, 3337–3390.
33 G. Te Velde, F. M. Bickelhaupt, E. J. Baerends, C. Fonseca Guerra, S. J. A. Van Gisbergen, J. G. Snijders and T. Ziegler, *J. Comput. Chem.*, 2001, **22**, 931–967.
34 E. Van Lenthe and E. J. Baerends, *J. Comput. Chem.*, 2003, **24**, 1142–1156.
35 E. Van Lenthe, A. Ehlers and E. J. Baerends, *J. Chem. Phys.*, 1999, **110**, 8943–8953.
36 E. Van Lenthe, E. J. Baerends and J. G. Snijders, *J. Chem. Phys.*, 1993, **99**, 4597–4610.
37 T. Lu and F. W. Chen, *J. Comput. Chem.*, 2012, **33**, 580–592.
38 G. X. Tian, Y. J. Zhu, J. M. Xu, P. Zhang, T. D. Hu, Y. N. Xie and J. Zhang, *Inorg. Chem.*, 2003, **42**, 735–741.
39 K. Huang, X. Feng, X. M. Zhang, Y. T. Wu and X. B. Hu, *Green Chem.*, 2016, **18**, 1859–1863.
40 K. C. Sole and J. B. Hiskey, *Hydrometallurgy*, 1992, **30**, 345–365.
41 B. K. Tait, *Hydrometallurgy*, 1993, **32**, 365–372.
42 C. Bourget, B. Jakovljevic and D. Nucciarone, *Hydrometallurgy*, 2005, **77**, 203–218.
43 S. C. Herndon and A. R. Ravishankara, *J. Phys. Chem. A*, 2006, **110**, 106–113.
44 G. S. Tyndall and A. R. Ravishankara, *Int. J. Chem. Kinet.*, 1991, **23**, 483–527.
45 M. Z. Li, E. Karu, C. Brenninkmeijer, H. Fischer, J. Lelieveld and J. Williams, *npj Clim. Atmos. Sci.*, 2018, **1**, 1–7.
46 A. M. Thompson, *Science*, 1992, **256**, 1157–1165.
47 Y. X. Wang, J. M. Hao, M. B. Mcelroy, J. W. Munger, H. Ma, C. P. Nielsen and Y. Q. Zhang, *Tellus*, 2010, **62**, 228–241.
48 S. X. Hu, J. J. Liu, J. K. Gibson and J. Li, *Inorg. Chem.*, 2018, **57**, 2899–2907.
49 J. Q. Wang, C. X. Chi, H. S. Hu, L. Y. Meng, M. B. Luo, J. Li and M. F. Zhou, *Angew. Chem., Int. Ed.*, 2018, **57**, 542–546.
50 W. L. Li, T. T. Chen, D. H. Xing, X. Chen, J. Li and L. S. Wang, *Proc. Natl. Acad. Sci. U. S. A.*, 2018, **115**, E6972–E6977.
51 D. Y. Zubarev and A. I. Boldyrev, *J. Org. Chem.*, 2008, **73**, 9251–9258.

